Journal of Power Sources 285 (2015) 568–579

Contents lists available at ScienceDirect

Journal of Power Sources

journal homepage: www.elsevier.com/locate/jpowsour

Study of effective transport properties of fresh and aged gas diffusion layers

Magdalena Bosomoiu, Georgios Tsotridis, Tomasz Bednarek*

European Commission, Directorate-General Joint Research Centre, Institute for Energy and Transport, Postbus 2, 1755 ZG Petten, The Netherlands

HIGHLIGHTS

- The brand new, conditioned and aged GDL samples are reconstructed using CT to obtain the effective tensor material parameters.
- The effect of GDL compression by Bi-Polar plates' ribs is considered.
- The water saturation and its impact on GDL transport properties are investigated.

ARTICLE INFO

Article history:
Received 24 September 2014
Received in revised form
11 March 2015
Accepted 21 March 2015
Available online 24 March 2015

Keywords:
Gas diffusion layer degradation
Effective properties
Proton exchange membrane
Fuel cell
Computer tomography

ABSTRACT

Gas diffusion layers (GDLs) play an important role in proton exchange membrane fuel cells (PEMFCs) for the diffusion of reactant and the removal of product water. In the current study fresh and aged GDLs (Sigracet® GDL34BC) were investigated by X-ray computed tomography to obtain a representative 3D image of the real GDL structure. The examined GDL samples are taken from areas located under the flow channel and under the land. Additionally, a brand new Sigracet® GDL34BC was taken as a reference sample in order to find out the impact of fuel cell assembly on GDL. The produced 3D image data were used to calculate effective transport properties such as thermal and electrical conductivity, diffusivity, permeability and capillary pressure curves of the dry and partially saturated GDL. The simulation indicates flooding by product water occurs at contact angles lower than 125° depending on sample porosity. In addition, GDL anisotropy significantly affects the permeability as well as thermal and electrical conductivities. The calculated material bulk properties could be next used as input for CFD modelling of PEM fuel cells where GDL is usually assumed layer-like and homogeneous. Tensor material parameters allow to consider GDL anisotropy and lead to more realistic results.

1. Introduction

In recent years, the use of low temperature proton exchange membrane (PEM) fuel cells has increased considerably for automotive applications, back-up power units and small portable units because of their high efficiency, high power density, absence of emissions, low operating temperature and low noise. The single cell PEM fuel cell consists of one membrane electrode assembly (MEA) located between two flow plates with the role of providing the reactant gas access, controlling the temperature and collecting the current [1].

The Gas Diffusion Layer (GDL) is one of the components of the MEA and is placed at each side of the MEA. GDL is a support for catalyst but this study focuses on its transport properties. GDL plays an important role in gas transport from the flow channels to the catalyst layer, removal of the produced water, electron transport between catalyst layer and bi-polar plate and reaction heat removal. The GDL consists of carbon fibres that are impregnated with polytetrafluoroethylene (PTFE) to ensure that the hydrophobic character of the GDL is maintained.

The models developed for studying fuel cell performance are macroscopic models making simplifications of the real structure of the GDL [2–10]. Lemoine-Nava et al. [11] made an analysis of flooding and drying of the GDL and the catalyst layers by using a 1D transient two-phase flow model. It was shown that severe flooding of the GDL is mainly due to poor removal of liquid water (determined by the material properties) rather than to high water condensation rate, thereby highlighting the necessity to correctly

* Corresponding author.
E-mail address: Tomasz.Bednarek@ec.europa.eu (T. Bednarek).

http://dx.doi.org/10.1016/j.jpowsour.2015.03.132

estimate the material properties. Since water is produced in the cathode catalyst layer, there is a higher susceptibility of cathode side flooding. However, water has a controversial effect: too low content will have an adverse impact on fuel cell operation, causing an increase in ohmic resistance (due to the reduction in protonic conductivity of the membrane), while high water content will obstruct the diffusion path of the gases. In addition, due to the GDL anisotropy, the properties might vary significantly through plane and in-plane. Therefore, when performing computational fluid dynamics (CFD) modelling, the dependence of transport properties on the local saturation levels and on the structure of the material are very important to achieving reliable results.

The water management in PEM fuel cells was investigated in Refs. [12,13]. The morphology model was used to examining the effects of liquid water presence on the transport properties of the carbon paper GDL. The effects of porosity and fibre distribution on the effective thermal conductivity were also studied. Calculations of effective thermal conductivity and diffusion coefficient in case of MPL were the goals of the papers [14–16]. Stochastic models were used to make a 3D reconstruction of the GDL and MPL. The effects of internal structure of the GDL and MPL (Micro Porous Layer) on transport properties (e.g. diffusion coefficient and thermal conductivity) were investigated. The effects of porosity and fibre distribution on the effective thermal conductivity were studied by Zamel et al. [14]. It was found that thermal conductivity increases with decreasing of porosity and is highly dependent on fibre distribution.

Similar approach was shown by Becker et al. in Ref. [17] in case on MPL. The diffusivity results for reconstructed GDL material with various MPL thicknesses and without MPL were considered. A method was presented which allows to compute binary diffusivity for a range of Knudsen numbers.

Several of the above mentioned papers ([12–17]) deal with investigation of the effective properties for numerically generated GDL or MPL structures.

In order to better estimate the effective transport properties as a non-scalar properties, the 3D geometry of a real GDL should be used in simulations instead of artificially reconstructed structures. Such non-scalar quantities may subsequently be used in CFD calculations where the GDL is simply treated as a homogeneous layer of constant porosity. This would allow to perform 3D fuel cell simulations taking into account the anisotropy of fuel cell parts, especially GDL.

The main objective of this study is to show the influence of fuel cell assembly and ageing processes on the effective GDL transport parameters, such as: electrical and thermal conductivities, diffusivity, capillary pressure as well as gas permeability. Several liquid water saturation levels were also taken into consideration. The X-ray computed tomography technique (CT) was used to determine the 3D anisotropic structure of different GDL samples such as fresh and aged; located under the flow channel and under the land, at a resolution of 1.5 μm. The results of the two aged materials – taken from under the channel and under the land regions – were compared with the fresh ones. The effect of liquid water is studied by calculating the saturation dependence transport properties.

2. Preparation of samples

In this study three types of materials were used, namely: i) One type called "fresh". This material was extracted from the MEA that was installed in a fuel cell setup but never operated. The purpose of using this material was to study the effect of compression to the GDL. ii) The second type called "aged". This GDL was extracted from an MEA that was operated for 1000 h at varying loads between 20% and 100% of the maximum power. iii) The third type called "brand new". In contrast to the other materials, this GDL was not extracted from MEA. The brand new Sigracet® GDL34BC sample is taken from GDL sheet provided by SGL GROUP company [18].

The fresh and aged GDLs, as part of the MEAs, were installed in a fuel cell setup. The fuel cell was assembled by applying a torque of 10 Nm on each of the bolts of the fuel cell setup according to manufacturer requirements. During the assembly process some areas of the GDL are located under the channel and they are called thereafter "under channel", other ones are compressed by the Bi-Polar plates ribs and are called "under land", see Fig. 1.

A sample with a width of 3 mm and a length of 10 mm were cut from each MEAs, fresh as well as aged. In order to study the compression of the GDL effect on the bulk properties, the MEA samples were cut along the lines marked by the Bi-Polar plates during fuel cell assembly, which could be easily observed on the GDL surface. Such method of sample preparation allows the examination of the GDL located under the channel as well as under the land.

These MEA samples are investigated using an X-ray computer tomograph Phoenix Nanotom S system that includes a 180 kV nanofocus X-ray tube and a 2D X-ray detector with 120×120 mm active area (2300×2300 pixels). Since the diameter of MPL pores are of the order of nm [15] the resolution of the CT scan was not sufficient to reliably reproduce the MPL, therefore, the MPL was excluded from considerations in this study.

Excision of the MPL from Sigracet® GDL34BC implies that properties of Sigracet® GDL34BA could be taken into account. The only difference between Sigracet® GDL34BC and Sigracet® GDL34BA is the MPL. The"BC" marking means GDL with MPL whereas "BA" corresponds to GDL without MPL. The carbon paper layer is the same in both, "BC" and "BA" GDLs, see Fig. 1 [18].

The numerical images used in the simulations are taken from the cathode side of the MEAs by taking into account the under the channel and under the land areas. In order to avoid influence of MPL, possible membrane impregnation and surface effects (for example loose fibres) the 3D GDL models are taken from the middle of the scanned cathode GDL, see Fig. 1. Due to above mentioned reasons the thickness of the GDL numerical model is limited to 150 μm as compared to the thickness of brand new Sigracet® GDL34BC is 315 μm. The location of the investigated samples is shown in Fig. 1. The total size of each samples are $150 \times 600 \times 1200$ μm.

In total, there are four examined GDL samples taken from cathode side of fresh and aged MEAs, namely: fresh under channel, fresh under land, aged under channel and aged under land. Additionally, the brand new Sigracet® GDL34BC sample was taken as a

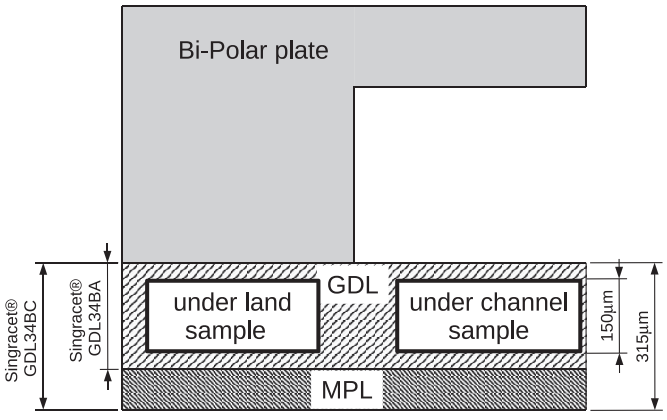

Fig. 1. The location of the investigated samples in the fuel cell setup.

reference in the case of comparing pore size distribution between brand new and fresh samples analysis.

3. Image analysis

Since the raw CT data is blurred, there is no clear surface distinction between solid structure and voids. The Modular Algorithms for Volume Images (MAVI) software [19] is used in order to find the clear surface which separates voids and solid structure of carbon fibres and to eliminate suspended particles which apparently do not correspond to the real structure.

The 3D images have bright voxels attributed to solid and dark voxels attributed to void space. A number of image manipulation filters and tools were used in reproduction of GDL structure.

Initially the mean filter is applied to reduce noise in the raw data. As a result the raw computer tomography image becomes smoother, hence resulting on smoothening of the fibres surfaces.

Next the segmentation (binarisation) is applied. Segmentation changes the grey scale image to a binary image: 0 means solid and 1 means void. The segmentation threshold is based on the histogram chart and the Otsu method [19].

As the last step of image manipulation a sequence of erosion and dilatation filters are applied to eliminate suspended particles. In general, the erosion filter changes the value of the central pixel of the structuring element (cube) to the minimum grey value of all pixels covered by the structuring element mask. For binary images (pixels take value of 0 or 1) erosion filter reduces the number of foreground pixels. On the other hand, dilatation filter changes the value of the central pixel of the structuring element to the maximum grey value of all pixels covered by the element mask. Sample snapshots from the image manipulation process are shown in Fig. 2.

The full definition of used image filters and tools can be found in MAVI handbook [19].

Table 1
Average samples porosities.

Sample name	Porosity [%]
Brand new Sigracet® GDL34BC	75.0
Fresh GDL under channel	76.7
Fresh GDL under land	67.1
Aged GDL under channel	84.6
Aged GDL under land	80.2

Unfortunately the PTFE coating and carbon fibres (graphite) have similar densities (2200 $kg\ m^{-3}$ and 2090–2230 $kg\ m^{-3}$ respectively [20]), thus the presented method does not distinguish between carbon fibres and PTFE. Therefore, it is not possible to attribute different properties (i.e. thermal of electrical conductivity) due to PTFE content. The contribution of the current paper provides comparison between aged and fresh materials located under the land and under the channel. It is assumed that the PTFE has the same properties as the carbon fibres. Initially the PTFE content is 5% for the fresh sample (manufacturer specification [18]) and less than that for the aged samples due to its degradation during operation, for example by constant attacks of H^+ radicals.

4. Results and discussion

4.1. Pore size distribution

The GDL structure regenerated in MAVI is imported into GeoDict software [21] to calculate transport properties.

The average porosities of the investigated samples are given in Table 1. The calculated porosity of the brand new GDL sample agrees with the data sheet provided by manufacturer (75%) [22]. Generally, the porosity of the aged samples is higher than fresh ones.

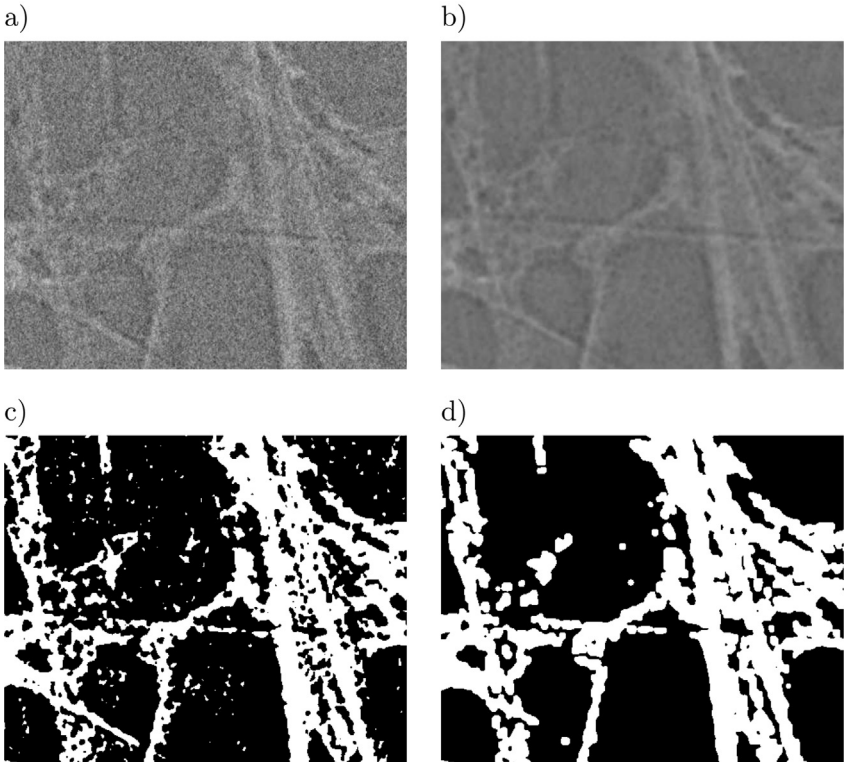

Fig. 2. The image manipulations from raw CT scan to binary image with solid/void structure: a) raw CT image, b) blurring by mean filter, c) after segmentation, d) final result.

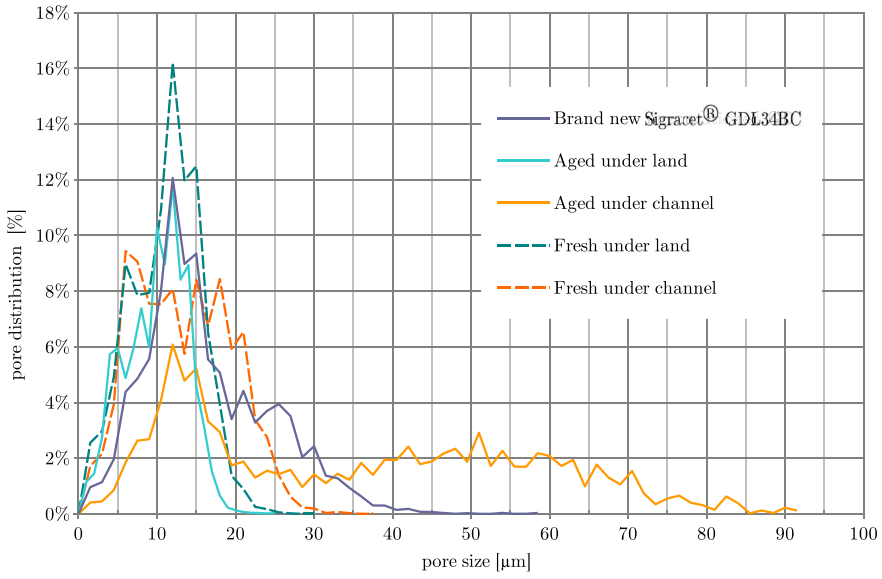

Fig. 3. Pore size distribution of the GDL samples.

Table 2
Thermal conductivity of anisotropic GDLs.

	Thermal conductivity [$W\ m^{-1}\ K^{-1}$]		
	X	Y	Z
Fresh under channel	0.908	7.619	6.107
Fresh under land	4.081	16.230	13.268
Aged under channel	1.074	4.096	6.011
Aged under land	1.428	4.918	7.781

A quantitative description of the pore size distribution is evaluated for each GDL sample, Fig. 3. Fresh under gas channel GDL sample has different pore distribution in comparison to the brand new GDL. It demonstrates that compression of the GDL by Bi-Polar plates during fuel cell assembly affects also the under channel area. Some pores are smaller while others become larger.

Table 3
Effective thermal conductivity in dependence of liquid water saturation in the GDL.

Liquid water saturation	Thermal conductivity [$W\ m^{-1}\ K^{-1}$]		
	X	Y	Z
Fresh under channel sample			
dry	0.908	7.619	6.107
25%	1.076	7.878	6.321
50%	1.379	8.207	6.577
75%	1.775	8.699	6.955
Fresh under land sample			
dry	4.081	16.230	16.230
25%	4.307	16.460	16.348
50%	4.729	16.808	16.710
75%	5.246	17.184	17.150
Aged under channel sample			
dry	0.607	2.144	3.099
25%	0.784	2.345	3.299
50%	1.042	2.600	3.538
75%	1.407	2.982	3.891
Aged under land sample			
dry	0.789	2.574	4.418
25%	0.963	2.792	4.546
50%	1.288	3.121	4.938
75%	1.686	3.477	5.415

As expected the GDL under the land samples is denser. There is nearly no pores larger than 20 μm in both cases, fresh as well as aged under land samples.

The pore distribution of the aged under the land sample is similar with the brand new sample, compare charts in Fig. 3. The ageing and compression have opposite effects in case of pore size distribution analysis.

The aged under channel sample pore distribution is affected mostly by ageing process. During fuel cell operation the GDL is exposed to adverse conditions, for example constant attacks of H^+ radicals. Therefore the carbon fibres and PTFE layer corrode. The products of degradation, such as broken fibres, suspended particles and other GDL degradation products are blown out by the air stream hence increasing the porosity of the aged GDL. That is one of the reasons of relatively flat distribution of pores in aged under the gas channel GDL see Fig. 2. There are large pores from Ref. 30 μm up to 85 μm which are not present in the fresh GDL. The occurrence of such large pores (in comparison to GDL thickness ~150 µm) could dramatically change the transport properties of aged GDL.

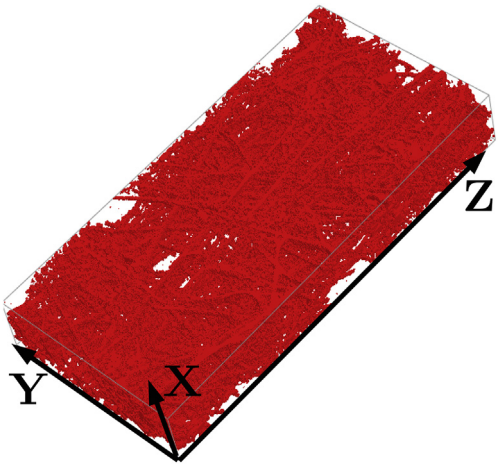

Fig. 4. The aged under channel sample with indicated coordinate system.

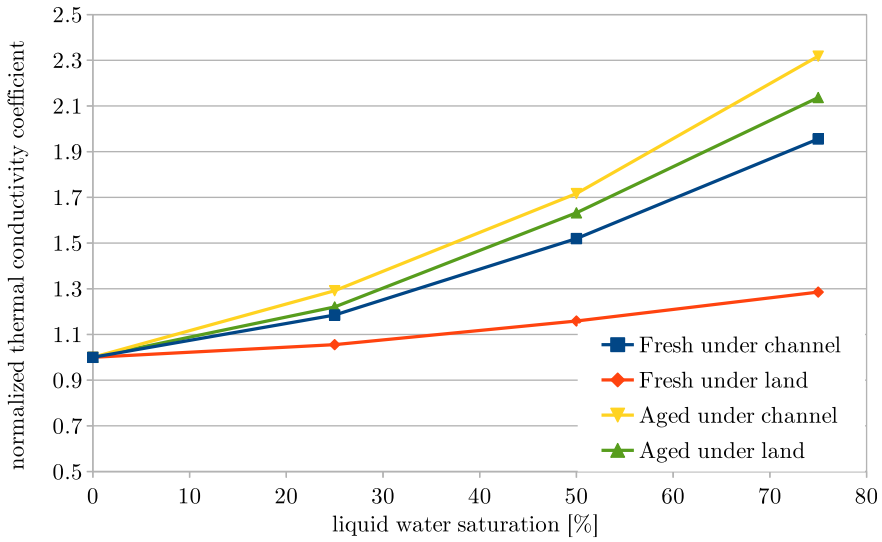

Fig. 5. The influence of liquid water saturation on normalized thermal conduction coefficient.

4.2. Effective thermal conductivity

The calculation of the effective transport properties of GDL requires the solution of the steady state equations of gas flow, heat transfer, diffusion of species and electric current [23]. Periodic boundary conditions were applied in all directions, which in principle consist of modelling a sample volume surrounded by the GDL structure.

The effective thermal conductivity $\mathbf{k}_{eff}$ is a tensor of the porosity ε, saturation s and the properties of the individual components; k_s and k_l are the thermal conductivity of the fibre and liquid water respectively, $\mathbf{k}_{eff} = f(k_s, k_l, \varepsilon, s)$.

To compute the effective thermal conductivity, the thermal conductivities of individual phases are required at a typical fuel cell operating temperature of 65 °C. Here the conductivities of carbon fibres and water are $k_s = 128.95\ W\ m^{-1}\ K^{-1}$ and $k_l = 0.6504\ W\ m^{-1}\ K^{-1}$ respectively [20,24]. Note also that water is taken as immovable droplets inside the GDL, thus the convection was neglected.

The model of heat transfer through the GDL takes into account conduction only. Heat transfer by radiation is neglected since the normal operating temperature of PEM fuel cell is lower than 100 °C. The contribution of various heat conduction capacities to the effective thermal conductivity of the GDL can therefore be obtained from

$$\mathbf{q} = -\mathbf{k}_{eff}\nabla T; \quad \mathbf{k}_{eff} = \begin{bmatrix} k_{xx} & k_{xy} & k_{xz} \\ k_{yx} & k_{yy} & k_{yz} \\ k_{zx} & k_{zy} & k_{zz} \end{bmatrix} \tag{1}$$

where $\mathbf{q}$ represents the heat flux and ∇T is the temperature gradient.

Table 4
Electrical conductivity of anisotropic GDLs.

	Electrical conductivity [$S\ m^{-1}$]		
	X	Y	Z
Fresh under channel	240.8	1619.6	2020.8
Fresh under land	1082.4	3519.0	4305.4
Aged under channel	284.9	1085.9	1593.8
Aged under land	368.6	1303.9	2063.6

The heat conduction equation is solved to obtain the heat flux $\mathbf{q}$ through the GDL

$$\nabla \cdot (k\nabla T) = 0 \tag{2}$$

where k is the local thermal conductivity and is dependent on the position in the computational domain. Calculation of heat flux $\mathbf{q}$ was performed by EJ-Heat solver implemented in GeoDict software [12,21].

Four values of liquid water saturation were assumed: 0% which correspond to a perfectly dry GDL, 25%, 50% and 75%. The obtained saturation-dependent thermal conductivities are given in Table 3 for the three main directions – Y and Z are in-plane directions while X is through plane direction, see Fig. 4. The X-direction saturation-dependent thermal conductivity values are smaller than those in Y- and Z-directions. The reason for this difference could be attributed to the direction of fibres – the thermal conductivity of the single fibre is grater along the fibre axis than across. Nearly all fibres are positioned in the Y-Z plane, but fibres are aligned in Z-direction more likely than in Y-direction. As expected, the corresponding value for thermal conductivity in Z-direction is the highest. This trend is similar for the aged samples but the values differ because of the different internal structure, porosity and compression levels. A significant effect of compression is observed at the thermal conductivity in the X-direction (through plane) as well as the Z- and Y-directions (in plane). The main reason is the

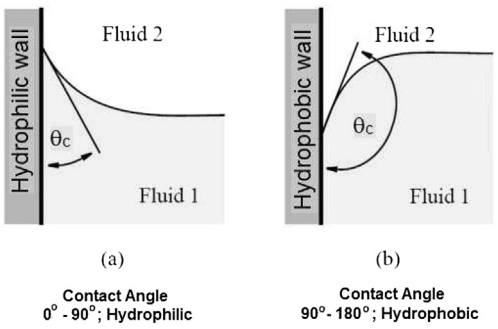

Fig. 6. GDL wettability (a) Fluid 1: wetting phase; Fluid 2: non-wetting phase; (b) Fluid 1: non-wetting phase; Fluid 2: wetting phase.

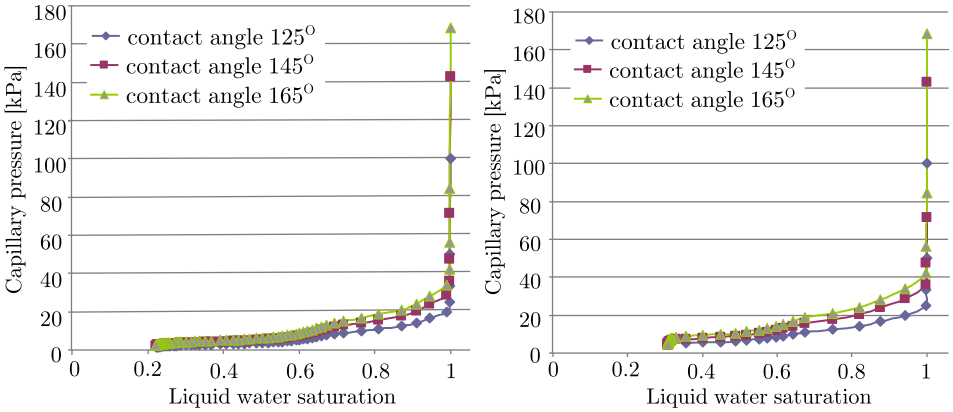

Fig. 7. Capillary pressure inside GDL for different contact angles during imbibition (left – aged GDL under channel; right – aged GDL under land). Unity means full saturation.

increasing number of contact points between fibres.

The influence of liquid water saturation on thermal conduction coefficient is presented in Fig. 5. The normalized thermal conduction coefficient k_{xx}^{N} is obtained by formula

$$k_{xx}^{N} = \frac{k_{xx}^{sat}}{k_{xx}^{dry}} \tag{3}$$

where k_{xx}^{sat} and k_{xx}^{dry} are tensor elements obtained for partially saturated and dry the GDL samples. The presence of water droplets inside the GDL increases the thermal conductivity of GDL. Due to the fact that water conductivity is much smaller than graphite conductivity the highest impact of water presence is noticed for specimens with higher porosity.

The diagonal values of thermal conductivity tensor for fresh and aged samples are presented in Table 2. The thermal conductivity tensor allows to take into account anisotropy of the GDL in numerical simulations of fuel cells, for example Fluent. The complete set of thermal conductivity tensors for all samples are shown in Appendix.

4.3. Electrical conductivity

In calculating the effective electrical conductivity $\boldsymbol{\sigma}_{eff}$, the electron flow through the GDL is considered. The GeoDict [21] is used to solve Ohm's law which relates the electric potential φ_s and the magnitude of current density $\mathbf{J}$.

$$\mathbf{J} = -\boldsymbol{\sigma}_{eff}\nabla\varphi_s; \quad \boldsymbol{\sigma}_{eff} = \begin{bmatrix} \sigma_{xx} & \sigma_{xy} & \sigma_{xz} \\ \sigma_{yx} & \sigma_{yy} & \sigma_{yz} \\ \sigma_{zx} & \sigma_{zy} & \sigma_{zz} \end{bmatrix} \tag{4}$$

As in case of thermal conductivity (Section 4.2) the conductivity equation is solved

$$\nabla \cdot (\sigma \nabla \varphi_s) = 0 \tag{5}$$

where σ is a local electrical conductivity dependent on the position in the domain.

The electrical conductivity of graphite at 65 $^{\circ}C$ is considered to be 34200 $S\ m^{-1}$ while the air conductivity is negligible as ($10^{-15}\ S\ m^{-1}$) [25].

The Sigracet® data sheet [18] [1] shows that the electrical conductivity of the brand new GDL 34BC compressed under pressure of 1.0 *MPa* (according to their data sheet) is not more than 909.09 $S\ m^{-1}$. However, it is difficult to estimate the compression pressure for the under land area. The clamping pressure is about 2.8 *MPa*, but it should be noticed that this clamping pressure is applied on both the MEA and the gasket as well. As result, it could be assumed that the clamping pressure applied to under the land specimens is grater than 1.0 *MPa* but not great enough to damage the GDL. The thus calculated through plane electric conductivity of the fresh under the land specimen is equal to 1082.38 $S\ m^{-1}$ and is grater than the limit value provided by manufacturer. The difference (about 173 $S\ m^{-1}$) arises from the higher compression of the under land specimen.

The results of electrical conductivity calculations are presented in Table 4.

The electrical conductivity of the GDL is much higher in in-plane (Z- and Y-directions) than perpendicular to the main fibre orientation X-direction, see Fig. 4. The compression of GDL implies larger number of contact points among the fibres therefore the samples under the land have a higher electrical conductivity than under the channel samples.

Comparison between fresh and aged samples, demonstrates that ageing does not affect the through plane electric conductivity of under the channel samples despite the fact of fibre degradation. Therefore, in spite of larger porosity of aged GDL the number of contact points between the fibres through GDL thickness seems not to change. However, broken fibres lead to the smaller electrical conductivities in case of in-plane directions, Table 4.

4.4. Capillary pressure

The liquid water management plays a crucial role on PEM fuel cell performance. The fuel cell membrane needs to be well saturated by liquid water in order to make possible diffusion of hydrogen protons. However, since more liquid water is accumulated in the GDL during fuel cell operation, its performance decreases, among other factors, due to blockage of the gas diffusion pathways from the gas channel to the catalyst layer. The surface of the GDL carbon fibres should be as hydrophobic as possible for facilitating the liquid water removal. In principle, the contact angle of GDL fibres should be as large as possible. The geometrical interpretation of contact angle is shown in Fig. 6. This section concerns with examination of the ability to water accumulation in GDL depending on the GDL wettability.

The capillary pressure dependence on the liquid saturation is presented to determining the mass transport limitations in the GDL. The wettability of the porous GDL is introduced into the model through the contact angle between carbon fibres and liquid

[1] The data sheet [18] provides through plane electrical resistance <11 $m\Omega\ cm^{-2}$ which is here related to the unit $S\ m^{-1}$.

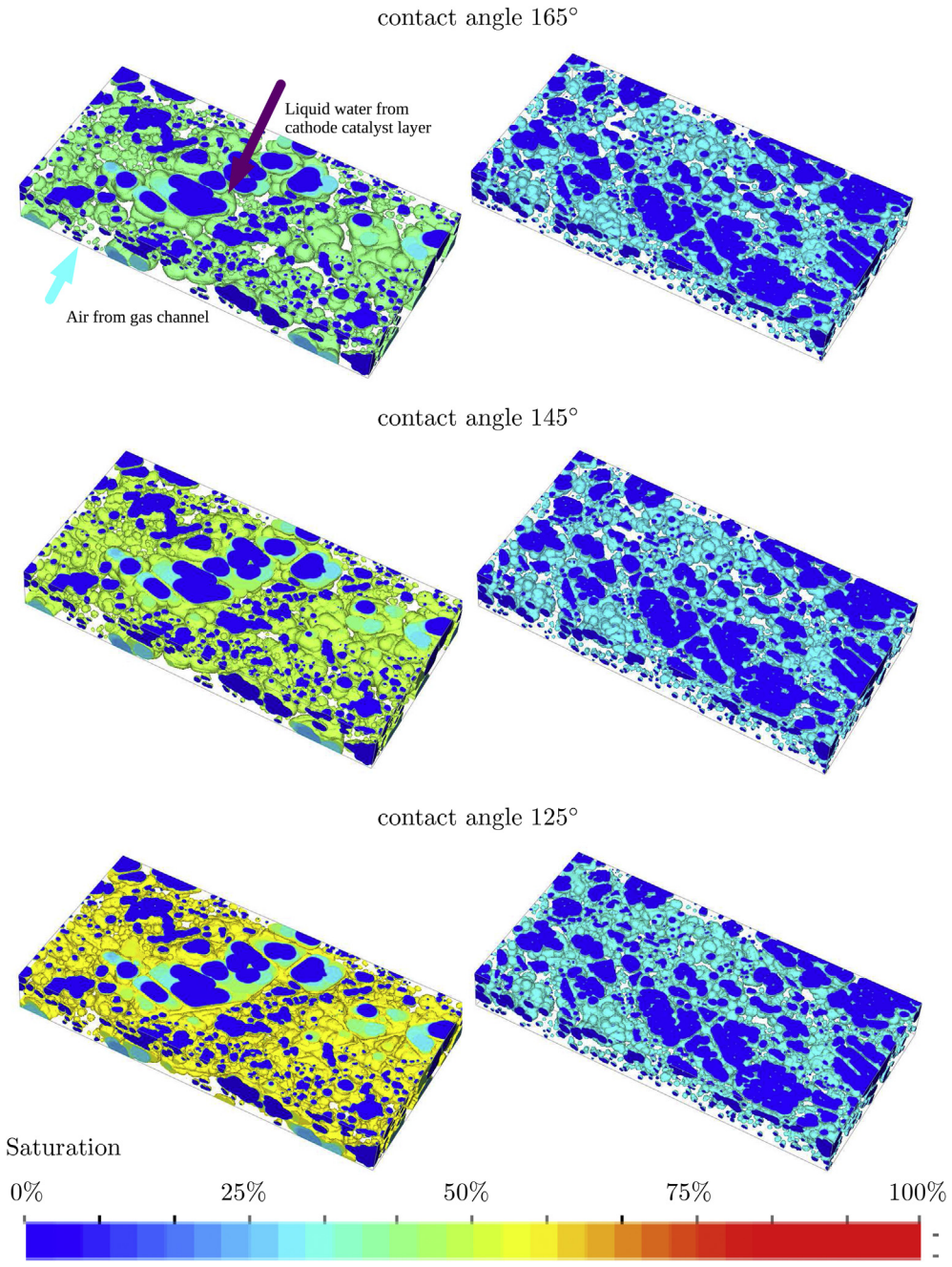

Fig. 8. Liquid water distribution inside the GDL for various contact angles (left – aged GDL under channel; right – aged GDL under land).

water (Fig. 6).

The intrusion of liquid water into GDL was simulated using pore-morphology-based model, widely described in Refs. [12,26,27]. The presence of liquid water is simulated by the determination of the quasi-static drainage curve of the wetting phase (i.e. gas) and its relationship with the capillary pressure. The method relies on specifying the radius of the spherical non-wetting fluid droplet (i.e. water) which is next compared with GDL pores. For a given water droplet radius, if the droplet can fit inside the pore, it is assumed that the pore is filled with water. Otherwise, if the pore is too small to fit the water droplet, the pore is assumed to be filled by wetting phase, i.e. gas.

The radius of spherical water droplet is then used for calculating the capillary pressure based on the by Eq. (6) [12]

Table 5
Effective diffusivity.

	Effective diffusivity [$\times 10^{-6}\ m^2\ s^{-1}$]		
	X	Y	Z
Fresh under channel	6.52	7.84	7.92
Fresh under land	4.21	5.87	6.11
Aged under channel	8.55	9.48	9.77
Aged under land	7.40	8.24	8.98

$$p_c = p_{nw} - p_w = p_l - p_g = -\frac{2\varsigma}{r}\cos\theta_c \tag{6}$$

Eq. (6) correlates the pore radius r accessible to the fluids and the capillary pressure p_c applied to the invading liquid water in order to

Table 6
Saturation dependent relative diffusivity.

Liquid water saturation	Relative effective diffusivity		
	X	Y	Z
Fresh under channel sample			
dry	0.49	0.58	0.59
25%	0.28	0.36	0.38
50%	0.12	0.17	0.20
75%	0.02	0.02	0.04
Fresh under land sample			
dry	0.31	0.43	0.45
25%	0.18	0.26	0.28
50%	0.06	0.12	0.13
75%	0.01	0.03	0.03
Aged under channel sample			
dry	0.63	0.70	0.72
25%	0.36	0.43	0.46
50%	0.15	0.20	0.24
75%	0.02	0.03	0.05
Aged under land sample			
dry	0.55	0.61	0.67
25%	0.32	0.37	0.41
50%	0.10	0.17	0.19
75%	0.02	0.04	0.05

penetrate the pore, θ_c is a contact angle and ς is surface tension. The subscripts: nw – non wetting phase, w – wetting phase, l – liquid water and g – gas phase. Calculations of capillary pressure were done using SatuDict, module of GeoDict Software [21].

During fuel cell operation, the GDL is progressively filled with condensed water transported from the cathode catalyst layer to the channel where it is suppose to be evacuated. In the simulation of the imbibition process, water enters the GDL through the top surface (Y-Z plane, see Fig. 4) while the air is evacuated through the opposite face. The process of water imbibition into GDL samples is stopped when capillary pressure of 5 *kPa* is achieved.

The capillary pressure versus liquid water saturation is calculated for various contact angles (165°, 145° and 125°) to account for the mass transport limitations in the GDL (Fig. 7). Since the contact angle of carbon fibres is not easy to be measured, the mentioned contact angles are uniform in the GDL and arbitrary chosen. The smaller contact angle implies lower pressure necessary for water intrusion into pores, therefore, the faster accumulation of water in the GDL.

The impact of contact angle on water accumulation in aged GDL is shown in Fig. 8. The aged samples located under channel and under land are presented on left and right hand side respectively. The white space represents the solid part of the GDL. For the aged under the channel sample with a contact angle of 165° the saturation level reaches about 40% (40% of the pores volume is occupied by liquid water). For 145° contact angle the liquid water increase to 45% while for 125° contact angle a further increase to about 60% is noticed. It could be seen that the colour of the droplets goes from green to yellow on the left hand side in Fig. 8. It means that more than half of the void GDL space is filled by liquid water when the contact angle is 125° or less, thus a drastic decrease of fuel cell performance is expected.

Among the three contact angles for under the land sample no significant differences of water saturation are observed. For contact angle 165° the maximum saturation is 30% while for contact angle 125° water saturation reaches a maximum of 35%.

From Fig. 7 it is concluded that the capillary pressure for under the channel GDL is lower than that under the land for a given water saturation level.

The current investigation provides capillary pressure curves which could be eventually used as input data for appropriate PEMFC numerical simulations.

4.5. Effective diffusivity

The effective diffusivity of GDL is calculated as an absolute value as well as relative diffusion coefficient specified in percentage terms, where 100% relative diffusion coefficient represents the diffusivity in an empty structure and 0% means no diffusion path is present or no empty volume is available.

In the pore space the diffusion is modelled by the equation

$$\nabla \cdot (D \nabla C) = 0 \tag{7}$$

where C is specie concentration and D is direction independent diffusion coefficient. In case of samples partially saturated by liquid water, the diffusion is simulated only in pores occupied by gas.

Solution of Eq. (7) gives the total diffusion flux **j**. The bulk diffusion tensor $\mathbf{D}_m$ can be next calculated with the Fick's law [15]

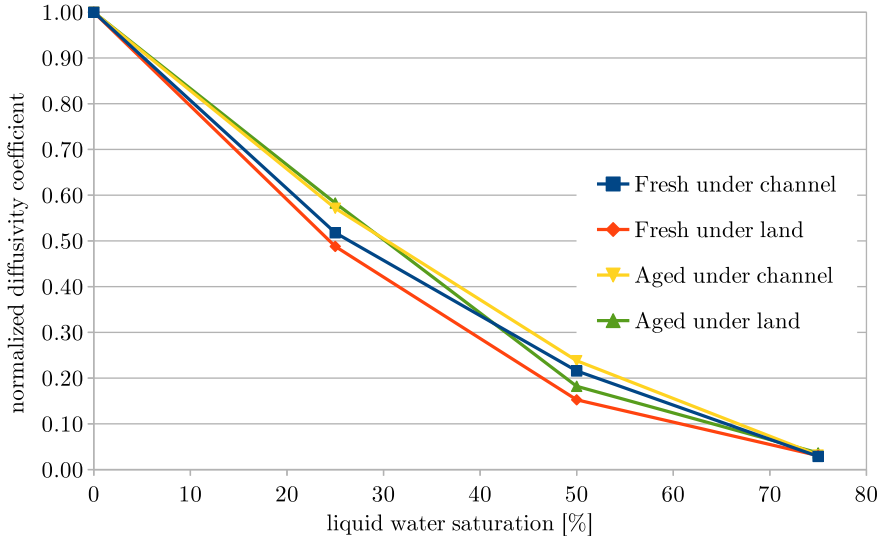

Fig. 9. The influence of liquid water saturation on the relative diffusivity coefficient through GDL plane (X-direction).

Table 7
Saturation dependent permeability.

Liquid water saturation	Effective permeability [$\times 10^{-12}$ m^2]		
	X	Y	Z
Fresh under channel sample			
dry	3.1	6.8	7.6
25%	1.3	4.5	4.8
50%	0.34	1.1	1.2
75%	0.024	0.099	0.11
Fresh under land sample			
dry	2.1	3.1	3.6
25%	0.65	0.72	0.76
50%	0.19	0.26	0.22
75%	0.042	0.043	0.024
Aged under channel sample			
dry	18.0	23.0	30.0
25%	4.8	6.5	7.8
50%	1.2	1.6	1.9
75%	0.086	0.14	0.18
Aged under land sample			
dry	6.3	11.0	18.0
25%	2.3	2.8	4.4
50%	0.69	1.0	1.3
75%	0.15	0.17	0.14

$$\mathbf{j} = -\mathbf{D}_m \nabla C \tag{8}$$

The diffusion process is simulated by DiffuDict module implemented in GeoDict software [21].

The dimensionless effective diffusivity was calculated using the mean thermal velocity ($\bar{v} = 497.13\ ms^{-1}$) – the average speed of the thermal motion of fluid particles and the mean free path of $\lambda = 8.128 \cdot 10^{-8} m$ – the average distance travelled by a moving particle between successive collisions at a specified temperature and pressure [24]. The effective diffusivity of air in the dry GDL is calculated by accounting for molecular diffusion, collision between air molecules as well as molecules with GDL fibres.

Molecular diffusion is modelled by applying a concentration gradient on the two opposite faces of the GDL. The simulations are repeated for two in-plane directions (Y and Z) and for through plane direction X, see Fig. 4.

The molecular diffusivity, D_m is calculated as the product between the dimensionless diffusivity of the matrix depending on the geometry of the GDL, D^*_{GDL} and the free bulk diffusivity of the diffusing fluid (air in this case), D'_m. D^*_{GDL} is independent of the fluid and describes the reduction in diffusivity due to the presence of the solid material (carbon fibres).

$$D_m = D'_m \cdot D^*_{GDL}. \tag{9}$$

The contribution of the fluid to the effective diffusivity is calculated by Ref. [23].

$$D'_m = \frac{1}{3}\lambda\bar{v}. \tag{10}$$

The diagonal elements of the calculated diffusion tensor for the fresh and aged samples are given in Table 5. The experimental values of the through plane molecular diffusivity of Sigracet® GDL 34BC is given in Ref. [28] and equals $5.9 \cdot 10^{-6}\ m^2\ s^{-1}$ and is comparable to the obtained value of $6.5 \cdot 10^{-6}\ m^2\ s^{-1}$. It should be mentioned that diffusivity measurements in Ref. [28] were performed at temperature 28 $^{\circ}C$ while current calculations were performed at higher temperature, namely 65 $^{\circ}C$.

The full tensors are given in Appendix, where it can be seen that the off-diagonal elements are about two orders of magnitude lower than the diagonal elements. It means, despite the fact of strong anisotropy of the GDL the diffusion occurs mostly in the main direction of species concentration gradient.

The major role of the GDL is to provide the reactants to the catalyst layer (by diffusion) and simultaneously to evacuate the fuel cell reaction products (vapour and liquid water) to the gas channel. Therefore, the relation between the diffusion coefficient of the GDL and the liquid water saturation is a key parameter to be considered by GFD modelling of fuel cells. Moreover, the diffusion process is affected by compression on the GDL exerted by the Bi-Polar plates ribs and by the liquid water saturation inside the GDL.

Effective diffusivity of partially saturated GDL is approximated in a tensor form by the equation

$$\mathbf{D}_i = \varepsilon^{1.5}(1-s)^{r_s}\mathbf{D}_i^0\left(\frac{p_0}{p}\right)^{\gamma_p}\left(\frac{T}{T_0}\right)^{\gamma_t} \tag{11}$$

which correspond to molecular diffusion at temperature T_0 and pressure p_0; r_s, γ_p and γ_t are exponents for respectively: pore blockage, pressure and temperature ($r_s = 2.5$, $\gamma_p = 1$, $\gamma_t = 1.5$,

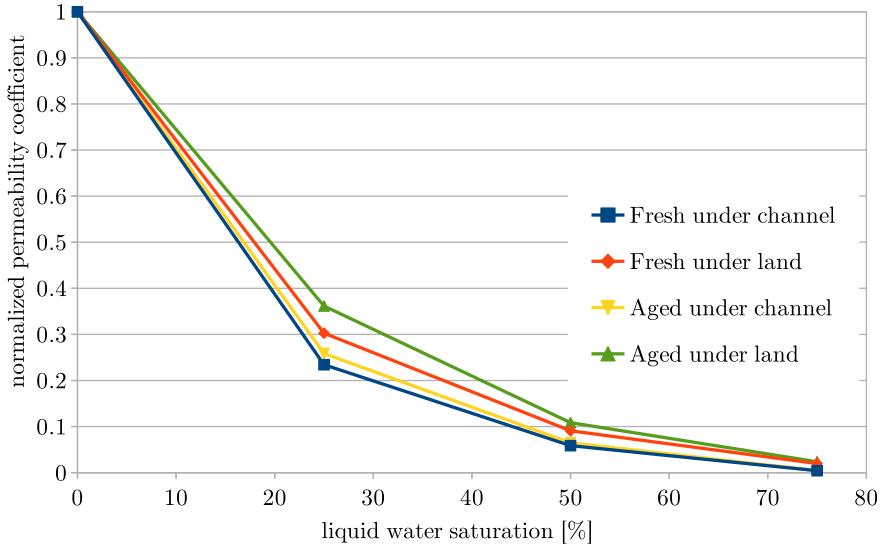

Fig. 10. The influence of liquid water saturation on relative permeability, through plane.

$p_0 = 101325\ Pa, T_0 = 300\ K$); ε is a volume fraction of the fluid phase and s is water saturation [29].

To quantify the decrease of effective diffusivity in the presence of liquid water in the GDL, the relative gas diffusivity coefficients are calculated for various saturation levels. The results indicate that even for small saturation levels (25%) a significant decrease of the through plane effective diffusivity by Ref. 57% in the most important flow direction – X (Table 6). 50% saturation drastically decreases the effective diffusivity by Ref. 85% in comparison with dry GDL. For saturation above 50% diffusion is virtually impaired for all samples.

The chart in Fig. 9 presents the normalized diffusion coefficient D^N_{xx}, obtained by

$$D^N_{xx} = \frac{D^{sat}_{xx}}{D^{dry}_{xx}} \tag{12}$$

where D^{sat}_{xx} and D^{dry}_{xx} are the coefficients obtained for partially saturated and dry (water free) GDL samples.

4.6. Permeability

The average flow velocity, needed for permeability calculations, is determined by solving the steady state Stokes equation, namely

$$-\mu\nabla^2 + \nabla P = 0, \quad \nabla \cdot \mathbf{u} = 0 \tag{13}$$

where μ is viscosity and $\mathbf{u}$ is fluid velocity. The pressure drop ∇P is taken as a boundary condition. The Eq. (13) is solved by FFF-Solver, part of GeoDict package [21].

The permeability of porous medium can be obtained by solving

$$\overline{v} = -\frac{K(s)}{\mu}\nabla P \tag{14}$$

where, $\overline{v}$ is the average flow velocity and $K(s)$ is the saturation dependent permeability. The flow occurs only through pores not occupied by liquid water. In other words water droplets are rigid and affect the flow in the same way as carbon fibres.

The calculated through plane permeability of fresh under channel GDL is equal $3.17 \cdot 10^{-12}\ m^2$. This value corresponds to values provided by SGL Group GDL properties data sheet [18].[2]

Similar to the diffusivity, permeability strongly depends on water saturation in the GDL. The calculation of permeability is based on pressure gradient applied to a GDL (partially) saturated with liquid water, Table 7 and Fig. 10. The critical decrease of GDL permeability appears when the water saturation level exceeds 50%. The reason is the same as in the case of decreased diffusivity. The largest pores, the easiest way to flow inside GDL, are occupied by liquid water. In result the gas goes mainly trough small pores with the higher flow resistance.

5. Conclusions

The structure of fresh and aged Sigracet® GDL34BC gas diffusion layers were reconstructed using X-ray CT to calculate material parameters as tensor quantities.

The performed simulations showed that the GDL compression by Bi-Polar plates during fuel cell assembly has an important effect both on pore diameter and on the effective properties, conductivity, diffusivity and permeability as well as ability to water accumulation inside GDL. The results obtained for the aged GDL sample under the channel (characterised by higher porosity) show the risk of a significant flooding (saturation level of 60%) at a contact angle of 125°. On the contrary, for the compressed aged sample the increase of liquid water saturation when changing the contact angle from Ref. 165° to 125° was lower.

For both aged samples a drastic decrease of the effective diffusivity by almost 90% is observed at 50% water saturation. Despite the fact of strong anisotropy of the GDL the diffusion occurs mostly in the main direction of species concentration gradient – the off-diagonal tensors elements are two orders of magnitude smaller that diagonal ones.

The electrical conductivity is quite different at the through plane (perpendicular to fibre orientation) and in-plane (along fibres orientation). Overall, it was shown that the degree of compression plays a significant role on the thermal and electrical conductivities of the GDL.

The calculated material properties could be used as input material properties for CFD modelling of PEM fuel cells resulting in more accurate calculations as contrary to the normal practice that is adopted in CFD modelling, where the GDL is usually assumed such as a homogeneous layer. With tensor material parameters GDL anisotropy can be considered to lead to more realistic results.

Acknowledgements

The authors would like to thank: CEA in Grenoble for providing the samples; Miguel Prieto and Algirdas Kersys from JRC for sample preparation and performing CT scans; Marc Steen and Thomas Malkow from JRC for critical reading of the manuscript.

Appendix. Macroscopic GDL tensors.

List of quantities

$\mathbf{k}_{eff}$	$W\ m^{-1}\ K^{-1}$	Effective thermal conductivity tensor
$\boldsymbol{\sigma}_{eff}$	$S\ m^{-1}$	Effective electrical conductivity tensor
$\mathbf{D}_m$	$m^2\ s^{-1}$	Molecular diffusivity tensor
$\mathbf{D}^r_m$	%	Relative diffusivity tensor
$\boldsymbol{\tau}$	–	Tortuosity vector
$\boldsymbol{\nu}$	m^2	Permeability tensor

Fresh GDL, under the channel, about 77% porosity, Eq. (15)[3]

$$\mathbf{k}_{eff} = \begin{bmatrix} 0.907756 & -0.00518631 & -0.182628 \\ -0.00513913 & 7.61916 & 0.649767 \\ -0.182756 & 0.649717 & 6.10661 \end{bmatrix} \tag{15}$$

$$\boldsymbol{\sigma}_{eff} = \begin{bmatrix} 240.77 & -1.37321 & -48.437 \\ -1.363 & 2020.75 & 172.331 \\ -48.4361 & 172.313 & 1619.59 \end{bmatrix} \tag{16}$$

[2] Since MPL is not considered the properties of Singracet® GDL34BA should be taken into account (see Section 2, page 2).The air permeability is provided in data sheet [18], namely the air permeability of Singracet ® GDL34BA (without MPL) equal $45\ cm\ s^{-1}$ is related to permeability and equals $3.65 \cdot 10^{-12}\ m^2$.

[3] The negative values for the off-diagonal tensor elements stem from periodic boundary conditions and the orientation of the global coordinate system used. A negative value means that the transport (of heat, species or electrons) happens opposite to the normal axis direction with respect to the global coordinate system.

$$\mathbf{D}_m = \begin{bmatrix} 6.56347 \cdot 10^{-6} & 1.02433 \cdot 10^{-7} & -4.5534 \cdot 10^{-8} \\ 1.02431 \cdot 10^{-7} & 7.96294 \cdot 10^{-6} & 2.65438 \cdot 10^{-8} \\ -4.5517 \cdot 10^{-8} & 2.65367 \cdot 10^{-8} & 7.87631 \cdot 10^{-6} \end{bmatrix} \quad (17)$$

$$\mathbf{D}_m^r = \begin{bmatrix} 48.7305 & 0.760517 & -0.338067 \\ 0.760501 & 59.1209 & 0.197075 \\ -0.337941 & 0.197022 & 58.4777 \end{bmatrix} \quad (18)$$

$$\boldsymbol{\tau} = [1.573432415 \quad 1.296904893 \quad 1.311169267]^T \quad (19)$$

$$\boldsymbol{\nu} = \begin{bmatrix} 3.174113 \cdot 10^{-12} & 1.216835 \cdot 10^{-13} & -1.661110 \cdot 10^{-14} \\ 1.211229 \cdot 10^{-13} & 7.639460 \cdot 10^{-12} & -1.698959 \cdot 10^{-13} \\ -8.061206 \cdot 10^{-15} & -1.412413 \cdot 10^{-13} & 6.810647 \cdot 10^{-12} \end{bmatrix} \quad (20)$$

Fresh GDL, under the land, about 67% porosity

$$\mathbf{k}_{eff} = \begin{bmatrix} 4.08064 & 0.0794654 & -0.0619508 \\ 0.0794559 & 16.2302 & 0.71609 \\ -0.0619233 & 0.716131 & 13.2683 \end{bmatrix} \quad (21)$$

$$\boldsymbol{\sigma}_{eff} = \begin{bmatrix} 1082.38 & 21.2955 & -16.392 \\ 21.0482 & 4305.35 & 189.869 \\ -16.3882 & 189.3 & 3519.0 \end{bmatrix} \quad (22)$$

$$\mathbf{D}_m = \begin{bmatrix} 4.24797 \cdot 10^{-6} & 2.02879 \cdot 10^{-8} & -4.72531 \cdot 10^{-8} \\ 2.05503 \cdot 10^{-8} & 6.14939 \cdot 10^{-6} & 2.66482 \cdot 10^{-8} \\ -4.72704 \cdot 10^{-8} & 2.70434 \cdot 10^{-8} & 5.90886 \cdot 10^{-6} \end{bmatrix} \quad (23)$$

$$\mathbf{D}_m^r = \begin{bmatrix} 31.5391 & 31.5391 & -0.350831 \\ 0.152576 & 45.6562 & 0.197849 \\ -0.35096 & 0.200784 & 43.8704 \end{bmatrix} \quad (24)$$

$$\boldsymbol{\tau} = [2.128693353 \quad 1.47049085 \quad 1.530348468]^T \quad (25)$$

$$\boldsymbol{\nu} = \begin{bmatrix} 2.140647 \cdot 10^{-12} & 3.099583 \cdot 10^{-14} & -3.000356 \cdot 10^{-14} \\ 2.243159 \cdot 10^{-14} & 3.617320 \cdot 10^{-12} & 6.753903 \cdot 10^{-15} \\ -4.139675 \cdot 10^{-14} & 6.643915 \cdot 10^{-15} & 3.190541 \cdot 10^{-12} \end{bmatrix} \quad (26)$$

Aged GDL, under the channel, about 85% porosity

$$\mathbf{k}_{eff} = \begin{bmatrix} 1.07437 & 0.182976 & -0.100222 \\ 0.182519 & 4.09573 & 0.331104 \\ -0.100459 & 0.331196 & 6.01066 \end{bmatrix} \quad (27)$$

$$\boldsymbol{\sigma}_{eff} = \begin{bmatrix} 284.942 & 48.5288 & -26.5807 \\ 48.4074 & 1086.27 & 87.8152 \\ -26.6436 & 87.8396 & 1594.14 \end{bmatrix} \quad (28)$$

$$\mathbf{D}_m = \begin{bmatrix} 8.54806 \cdot 10^{-6} & 1.87908 \cdot 10^{-7} & -8.25484 \cdot 10^{-8} \\ 1.88379 \cdot 10^{-7} & 9.49308 \cdot 10^{-6} & 2.33279 \cdot 10^{-8} \\ -8.25474 \cdot 10^{-8} & 2.29435 \cdot 10^{-8} & 9.76686 \cdot 10^{-6} \end{bmatrix} \quad (29)$$

$$\mathbf{D}_m^r = \begin{bmatrix} 63.4652 & 1.39513 & -0.612881 \\ 1.39862 & 70.4814 & 0.173198 \\ -0.612873 & 0.170344 & 72.5141 \end{bmatrix} \quad (30)$$

$$\boldsymbol{\tau} = [1.334120265 \quad 1.201311962 \quad 1.167636582]^T \quad (31)$$

$$\boldsymbol{\nu} = \begin{bmatrix} 1.857093 \cdot 10^{-11} & 1.257918 \cdot 10^{-12} & -1.183699 \cdot 10^{-12} \\ 1.244870 \cdot 10^{-12} & 2.367411 \cdot 10^{-11} & 1.32939 \cdot 10^{-12} \\ -1.182663 \cdot 10^{-12} & 1.271353 \cdot 10^{-12} & 2.987740 \cdot 10^{-11} \end{bmatrix} \quad (32)$$

Aged GDL, under the land, about 80% porosity

$$\mathbf{k}_{eff} = \begin{bmatrix} 1.42773 & 0.0169069 & 0.478988 \\ 0.0153062 & 4.91775 & 0.0514345 \\ 0.501562 & 0.0498813 & 7.78133 \end{bmatrix} \quad (33)$$

$$\boldsymbol{\sigma}_{eff} = \begin{bmatrix} 378.66 & 4.48403 & 127.037 \\ 4.05949 & 1304.28 & 13.6414 \\ 133.024 & 13.2295 & 2063.76 \end{bmatrix} \quad (34)$$

$$\mathbf{D}_m = \begin{bmatrix} 7.39936 \cdot 10^{-6} & 7.8111 \cdot 10^{-8} & 1.11056 \cdot 10^{-7} \\ 7.81062 \cdot 10^{-8} & 8.24064 \cdot 10^{-6} & -3.06466 \cdot 10^{-8} \\ 1.11075 \cdot 10^{-7} & -3.05965 \cdot 10^{-8} & 8.98431 \cdot 10^{-6} \end{bmatrix} \quad (35)$$

$$\mathbf{D}_m^r = \begin{bmatrix} 54.9366 & 0.579936 & 0.824534 \\ 0.5799 & 61.1827 & -0.227536 \\ 0.82468 & -0.227164 & 66.7041 \end{bmatrix} \quad (36)$$

$$\boldsymbol{\tau} = [1.460093956 \quad 1.311034986 \quad 1.20251479]^T \quad (37)$$

$$\boldsymbol{\nu} = \begin{bmatrix} 6.362959 \cdot 10^{-12} & -9.67438 \cdot 10^{-14} & 1.705170 \cdot 10^{-13} \\ -9.861081 \cdot 10^{-14} & 1.046605 \cdot 10^{-11} & -4.149783 \cdot 10^{-14} \\ 2.015145 \cdot 10^{-13} & 6.949687 \cdot 10^{-14} & 1.763852 \cdot 10^{-11} \end{bmatrix} \quad (38)$$

References

[1] S. Srinivasan, Fuel Cells from Fundamentals to Applications, Springer, 2006.
[2] T.F. Fuller, J. Newman, J. Electrochem. Soc. 140 (1993) 1218–1225.
[3] V. Gurau, H. Liu, S. Kaka, AIChE J. 44 (1998) 2410–2422.
[4] G.H. Guvelioglu, H.G. Stenger, J. Power Sources 147 (12) (2005) 95–106, 0378–7753.
[5] C. Ziegler, A. Schmitz, M. Tranitz, E. Fontes, J.O. Schumacher, J. Electrochem. Soc. 151 (2004) A2028–A2041.
[6] J.S. Yi, T.V. Nguyen, J. Electrochem. Soc. 145 (1998) 1149–1159.
[7] T. Berning, M. Odgaard, S. Kær, J. Power Sources 196 (15) (2011) 6305–6317, 0378–7753.
[8] S. Dutta, S. Shimpalee, J.V. Zee, Int. J. Heat Mass Transf. 44 (11) (2001) 2029–2042, 0017–9310.
[9] A.D. Le, B. Zhou, J. Power Sources 193 (2) (2009a) 665–683, 0378–7753.
[10] A.D. Le, B. Zhou, Electrochim. Acta 54 (8) (2009b) 2137–2154, 0013–4686.
[11] R. Lemoine-Nava, R. Hanke-Rauschenbach, M. Mangold, K. Sundmacher, Int. J. Hydrog. Energy 36 (2) (2011) 1637–1653, 0360–3199.
[12] N. Zamel, X. Li, J. Becker, A. Wiegmann, Int. J. Hydrog. Energy 36 (9) (2011)

5466–5478, 0360–3199.
[13] V.P. Schulz, J. Becker, A. Wiegmann, P.P. Mukherjee, C.-Y. Wang, J. Electrochem. Soc. 154 (4) (2007) B419–B426.
[14] N. Zamel, X. Li, J. Shen, J. Becker, A. Wiegmann, Chem. Eng. Sci. 65 (13) (2010) 3994–4006, 0009–2509.
[15] N. Zamel, J. Becker, A. Wiegmann, J. Power Sources 207 (0) (2012) 70–80, 0378–7753.
[16] J. Becker, R. Flückiger, M. Reum, F.N. Büchi, F. Marone, M. Stampanoni, J. Electrochem. Soc. 156 (10) (2009) B1175–B1181.
[17] J. Becker, C. Wieser, S. Fell, K. Steiner, Int. J. Heat Mass Transf. 54 (78) (2011) 1360–1368, 0017–9310.
[18] Sigracet® GDL 34&35 Series Gas Diffusion Layer – Datasheet, 23/10/2014. Available at: www.sglgroup.com/cms/international/infokorb/Downloadcenter/index.html?__locale=en#.
[19] Modular Algorithms for Volume Imaging (MAVI). Handbook, Fraunhofer ITWM, Kaiserslautern, Germany, 2001 available at: www.itwm.fraunhofer.de.
[20] B. Poling, J. Prausnitz, J. OConnell, Chemical Properties Handbook, McGraw-Hill, 2001.
[21] Fraunhofer ITWM, Department Flow and Complex Structures, GeoDict., Kaiserslautern, Germany, 2014 available at: www.itwm.fraunhofer.de.
[22] Gas Diffusion Layer Comparison Table, 23/10/2014. Available at: fuelcellsetc.com/store/DS/gas-diffusion-layer-properties.pdf.
[23] R. Bird, W. Stewart, E. Lightfoot, Transport Phenomena, John Willey & Sons, 1960.
[24] C. Yaws, Chemical Properties Handbook, McGraw-Hill, 1999.
[25] M. Miao, Carbon 49 (12) (2011) 3755–3761, 0008–6223.
[26] H.-J. Vogel, J. Tölke, V.P. Schulz, M. Krafczyk, K. Roth, Vadose Zone J. 4 (2005) 380–388.
[27] M. Hilpert, C.T. Miller, Adv. Water Resour. 24 (34) (2001) 243–255, 0309–1708.
[28] L.M. Pant, Experimental and Theoretical Investigation of Mass Transport in Porous Media of a PEM Fuel Cell, Master's thesis, Faculty of Graduate Studies and Research, University of Alberta, Canada, 2011.
[29] S. Um, C. Wang, K. Chen, J. Electrochem. Soc. 147 (2000) 4485–4493.